PCCP

PAPER

View Article Online
View Journal | View Issue

Boron doped defective graphene as a potential anode material for Li-ion batteries†

Cite this: *Phys. Chem. Chem. Phys.*, 2014, **16**, 16502

Rahul P. Hardikar,[a] Deya Das,[a] Sang Soo Han,[b] Kwang-Ryeol Lee[b] and Abhishek K. Singh*[a]

Received 1st April 2014,
Accepted 26th June 2014

DOI: 10.1039/c4cp01412j

www.rsc.org/pccp

Graphene with large surface area and robust structure has been proposed as a high storage capacity anode material for Li ion batteries. While the inertness of pristine graphene leads to better Li kinetics, poor adsorption leads to Li clustering, significantly affecting the performance of the battery. Here, we show the role of defects and doping in achieving enhanced adsorption without compromising on the high diffusivity of Li. Using first principles density functional theory (DFT) calculations, we carry out a comprehensive study of diffusion kinetics of Li over the plane of the defective structures and calculate the change in the number of Li atoms in the vicinity of defects, with respect to pristine graphene. Our results show that the Li–C interaction, storage capacity and the energy barriers depend sensitively on the type of defects. The un-doped and boron doped mono-vacancy, doped di-vacancy up to two boron, one nitrogen doped di-vacancy, and Stone–Wales defects show low energy barriers that are comparable to pristine graphene. Furthermore, boron doping at mono-vacancy enhances the adsorption of Li. In particular, the two boron doped mono-vacancy graphene shows both a low energy barrier of 0.31 eV and better adsorption, and hence can be considered as a potential candidate for anode material.

1 Introduction

Since the first commercialization of Li-ion batteries (LIBs), much research effort has been focused on increasing the capacity and performance of these batteries.[1–5] LIBs, which work on the principle of intercalation of Li^+ ions during charging–discharging cycles, heavily rely on better kinetics and capacity of the anode–cathode material. Current generation of LIBs mainly use graphite as the anode material due to its well-defined layered structure, chemical tolerance, broad electrochemical window in addition to excellent electrical properties.[6,7] Despite these properties, graphite shows a low specific capacity of 372 mA h g^{-1} (LiC_6),[8,9] which is not sufficient for providing the energy density required for future generation of portable electronics and hybrid electric vehicles.

Recently, graphene has been widely studied for application as anode material,[10–13] due to its high surface area and favourable electronic properties. Moreover, the sp^2 hybridized bonds in graphene provide good structural integrity, essential for anode materials. Experimentally, high specific capacity in the range of 900–1264 mA h g^{-1} was found for multi-layers (≥ 4) of high quality of graphene sheets.[10] However, *in situ* Raman spectra studies show that the amount of lithium absorbed on a single layer of graphene is significantly low compared to few layers.[14] Due to low adsorption of Li and agglomeration caused by strong Li–Li interaction,[15,16] pristine graphene is not a good choice for anode materials.

Alternatively, Li adsorption and storage capacity of graphene can be improved by introducing intrinsic or extrinsic defects.[17–19] The presence of defects, such as mono-vacancy, di-vacancy, and Stone–Wales, in the graphene matrix alters the electronic properties, creating active sites for Li adsorption. The rearrangement of atoms in the vicinity of the defect leads to improved binding of Li with the defects.[20] Substitutional doping in graphene with atoms such as boron (B)[21] and nitrogen (N)[22] can also provide higher capacity.[23,24] With comparable sizes, B/N doping[25] preserves the hexagonal structure of graphene[26] and avoids crystallization of dopant atoms. B doped graphene[27] shows good structural integrity and hence can also serve as protective material at high temperature for the anode.[28] It has been shown that highly B-doped graphene (B : C ratio in BC_3) does not form clusters of dopant atoms and maintains a 2D planar structure like graphene.[15] B substitution creates an electron deficient lattice,[29] while N doping gives an electron rich structure. Experimental evidence shows that the electrochemical performance of N- and B-doped graphene is better even at lower current rates and to some extent suppresses the decomposition of electrode material.[23]

[a] *Materials Research Centre, Indian Institute of Science, Bangalore 560012, India. E-mail: abhishek@mrc.iisc.ernet.in*
[b] *Korea Institute of Science and Technology, Hwarangno 14-gil 5, Seongbuk-gu, Seoul 136-791, Korea*

† Electronic supplementary information (ESI) available. See DOI: 10.1039/c4cp01412j

N doped graphene nanosheets (N-GNS) show a high reversible capacity of 684 mA h g^{-1}.[30] A very high theoretical capacity of 2271 mA h g^{-1} has also been realized in one of the phases of B doped graphene, BC_5.[31] Boron doped graphitic structures show higher reversible capacity and better cycle efficiency compared to un-doped analogs.[32,33]

For the defective graphene to be considered as promising anode material, along with better capacity it should also exhibit good diffusion kinetics for Li. Diffusion of Li in an anode can occur in two ways, (i) through and (ii) over (across) the plane (henceforth referred to as the basal plane[34]) of graphene. A recent study concluded that energy barriers for Li to diffuse through the basal plane of doped defective graphene are very high, except in di-vacancy defects (1.34 eV) and the boron doped di-vacancy case.[35] Here, we conduct a comprehensive study of the diffusion mechanism of Li over the basal plane of (a) defective, (b) doped and (c) doped defective graphene and calculate the number of adsorbed Li in the vicinity of these defects. We find that the energy barriers for diffusion over the basal plane are very low compared to the through diffusion barriers for respective structures. We observe moderately low energy barriers ($\leq$0.7 eV) for un-doped defective graphene, such as mono-vacancy, di-vacancy and Stone–Wales defects. Doping mono-vacancy with N leads to high energy barriers compared to the B doped graphene. Higher adsorption energy in N doped di-vacancy leads to high energy barriers in comparison with doped mono-vacancy. Boron doping at mono-vacancy also increases the Li uptake in the vicinity of the defects. In particular, the two B doped mono-vacancy gives a low energy barrier and enhanced Li uptake capacity, emerging as a potential anode material.

2 Methodology

We perform first principles calculations using *Vienna ab-initio Simulation Package* (VASP).[36,37] Electron–ion interactions and electronic exchange correlations were approximated by all-electron projector augmented wave potentials (PAW)[38] and the Perdew–Burke–Ernzerhof (PBE) generalized gradient approximation (GGA),[39,40] respectively. To simulate the diffusion over the basal plane of graphene, we use finite clusters of defective and doped defective structures with 50–54 C atoms, passivated by hydrogen at the edges. A conjugate gradient scheme was used to relax the structures until the components of the forces on each atom were of the order of 10^{-3} eV $Å^{-1}$. The cut-off energy is set to 400 eV to ensure the accuracy of the results. The periodic images were separated by 15 Å along all directions to avoid any image–image interactions. The Brillouin zone was sampled at the Γ point for all calculations. Single point calculations, being computationally inexpensive, are first employed to get an estimate of the low energy barriers for all possible symmetrically non-equivalent paths. Energy barriers for one of such paths, which includes the saddle point, are re-calculated using a more accurate Nudged Elastic Band (NEB) method.[41] In the NEB method, two local minima positions were chosen from the single point calculations and intermediate images were created by interpolating between these points or by choosing images from the single point calculations. With a sufficient number of images, the NEB method gives an accurate estimation of the saddle point. The intermediate images are then fully optimized ($3N - 1$ degrees of freedom) until the tangential force on each image achieves convergence. The co-ordinates of the relaxed structures of each image provide the minimum energy path and corresponding energy barriers are then calculated with respect to the energy of one Li relaxed on the molecule.

3 Results and discussion

We first build a formalism to achieve reliable estimates for diffusion barriers over the basal plane of graphene. Unlike diffusion of Li through the plane of graphene, the paths over the basal plane involve moving over bonds, atoms and hexagons, affecting the height of energy barriers. The energy of the relaxed structure containing one Li is considered as reference energy. The height of the energy barriers is calculated for different locations over the basal plane by considering the difference in energies with respect to the reference energy. In order to avoid any interaction of Li with edge passivated H atoms, the barrier heights are calculated within ~3 Å from the relaxed position of Li.

3.1 Kinetics of Li diffusion

Using the formalism discussed above, we first investigate the energy barriers for pristine and defective graphene. Fig. 1 shows a few representative across diffusion barriers corresponding to non-equivalent paths considered for scanning the potential

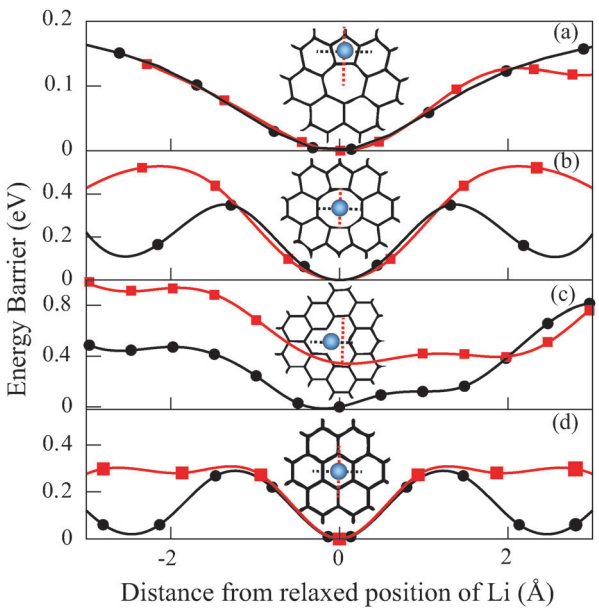

Fig. 1 Li diffusion barriers for (a) Stone–Wales, (b) di-vacancy, (c) mono-vacancy, and (d) pristine graphene, respectively. The insets show relaxed positions of Li over each structure. The black and red curves and corresponding dotted lines indicate energy barriers obtained for two representative non-equivalent paths across the basal plane of graphene. The red path in mono-vacancy is slightly shifted from the relaxed position of Li, hence finite barrier at a distance of zero.

energy surface for pristine, mono-vacancy, di-vacancy and Stone–Wales defective graphene with corresponding Li relaxed geometries. The red and black curves show energy barriers along two representative symmetrically non-equivalent paths considered between two local minima. As seen in Fig. 1(d), pristine graphene gives an energy barrier of 0.29 eV which is in good agreement with a previously reported value of 0.32 eV,[42] thus validating our approach.

Defective graphene. Introducing defects[43,44] can possibly hinder or facilitate the diffusion process. Our study reveals that the across diffusion barriers for defective graphene are much lower than the corresponding through diffusion barriers. For example, as shown in Fig. 1(c), mono-vacancy graphene gives an energy barrier of 0.49 eV, a significant improvement over through diffusion barrier (8.18 eV).[35] The energy barrier for across diffusion in di-vacancy graphene (Fig. 1(b)) is 0.35 eV, which is about 1 eV lower than the corresponding barrier for through diffusion. Another common defect seen in graphene is the Stone–Wales defect,[45,46] where the relaxed position of Li is slightly off-center over the pentagon. The asymmetric curve for the energy barrier, corresponding to the red arrow in Fig. 1(a), is due to diffusion of Li over pentagon followed by heptagon. A very low energy barrier of 0.13 eV is seen in the case of Stone–Wales defects. Among the un-doped pristine and defective graphene, the Stone–Wales defect shows the lowest energy barrier for Li diffusion. Thus, one can expect better kinetics, due to lowering of energy barriers, for the Li moving over the basal plane compared to the through diffusion.

In order to understand the origin of variations in energy barriers for across diffusion in defective graphene, we perform density of states (DOS) calculations. Fig. 2 shows partial density of states (PDOS) for Li (red), C (dark green) and total DOS (black), as a function of distance from the relaxed position of Li. We consider three different positions, far away (3.0 Å), the intermediate position (1.5 Å) of Li and at the relaxed position (0 Å) of Li, and investigate the change in DOS as shown in Fig. 2(a–c), respectively.

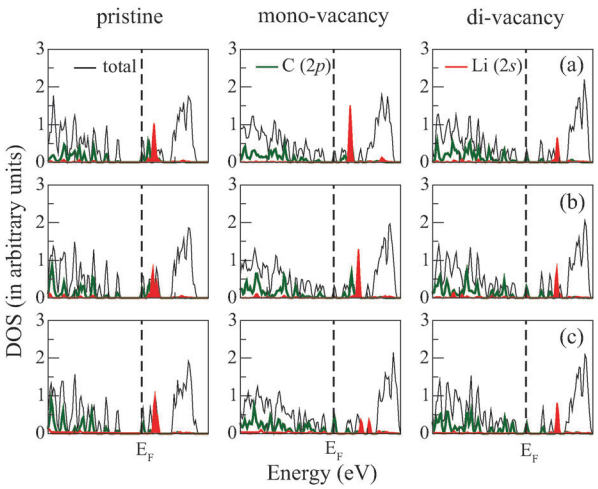

Fig. 2 Total and partial density of states of pristine, mono-vacancy and di-vacancy graphene plotted as a function of Li at (a) 3.0 Å, (b) 1.5 Å, and (c) 0 Å from the relaxed position of Li on each structure.

As Li approaches the defect sites, the Li-2s states in conduction bands are pushed to higher energy levels in the mono-vacancy, while there is a negligible shift in the case of pristine and di-vacancy. This indicates a greater interaction of Li with the mono-vacancy, potentially hindering the across diffusion. Hence, the energy barriers in pristine and di-vacancy are comparable, while the barrier for mono-vacancy is slightly higher.

Doped graphene. Experimentally, it has been shown that 3.06% of N-doping and 0.88% B doping in few layer graphene can give a very high capacity of 1043 mA h g^{-1} and 1549 mA h g^{-1}, respectively, at a low charge–discharge rate of 50 mA g^{-1}.[23] Next, we study the effect of extrinsic defects on the kinetics of Li by substituting C with B or N. Fig. 3(a) shows across energy barriers for B (open circles) and N (open squares) doped graphene. The barriers for across diffusion in B and N doped graphene are 0.73 eV and 0.45 eV, respectively. Doping graphene with B leads to an electron-deficient matrix and hence depicts stronger binding with the Li,[15,27] resulting in a slightly higher energy barrier. This is also evident from the PDOS plotted as a function of Li position from the doping site. As shown in Fig. 3(b–d), the Li-2s states shift to the higher energy levels in both B and N doped graphene. However, the shift is more in the B-doped case compared to the N-doped. Our observations are in agreement with a previous experimental study, where a shift in the Fermi level is seen because of B-doping and the effect on Li intercalation due to the presence of acceptor impurity.[47] To compare the stability of these structures with one Li, we calculate adsorption energy as

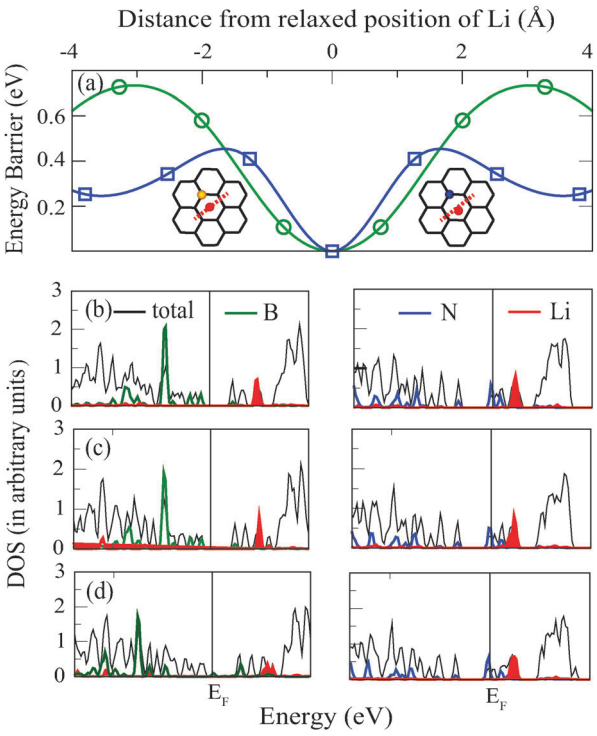

Fig. 3 (a) The Li diffusion barriers and corresponding relaxed structures with Li. Total and partial density of states of pristine B (green) and N (blue) doped graphene with Li at (b) 3.0 Å, (c) 1.5 Å, and (d) 0 Å from the relaxed position of Li.

shown in Table 2. Though the barrier in N doped graphene is lower, positive adsorption energy (0.75 eV) is not desirable since it can lead to clustering of Li.

Doped mono-vacancy defects. The above results clearly indicate that both defective and doped graphene can lower the energy barriers. As a consequence, we also consider the effect of doping on defective graphene. Table 1 gives a summary of energy barriers for several defective and doped defective graphene structures. Fig. 4(a) shows across diffusion as a function of B concentration at the mono-vacancy site. The open circle, square and diamond symbols correspond to one, two and three B doped graphene structures, respectively. There is a subsequent decrease of energy barriers, 0.44 eV and 0.31 eV, in mono-vacancy structures when doped with one and two B atoms. Though a slight reversal in the height of the barrier is seen with three B atoms (0.43 eV), overall the barriers for boron doped mono-vacancy are lower than the pristine mono-vacancy case. Thus, B doping on mono-vacancy has a positive effect on the across diffusion barrier. The diffusion path obtained by NEB is also tested by scanning the potential energy surface of two boron doped mono-vacancy defects. As shown in Fig. S1 (ESI†), the Li diffuses following the low energy path indicated by green contours below the potential energy surface. This path agrees well with NEB calculations.

Table 1 Energy barriers E_b (calculated using the NEB method) for across diffusion of Li over pristine, defective, B and N doped and defective graphene

System	E_b (eV)	System	E_b (eV)
Pristine	0.29	Mono-vacancy	0.49
Di-vacancy	0.35	SW defects	0.13
Pristine 1B	0.73	Pristine 1N	0.45
Mono 1B	0.44	Mono 1N	0.95
Mono 2B	0.31	Mono 2N	1.75
Mono 3B	0.43	Mono 3N	2.62
Di 1B	0.38	Di 1N	0.26
Di 2B	0.59	Di 2N	2.57
Di 3B	1.74	Di 3N	4.30
Di 4B	1.26	Di 4N	3.23

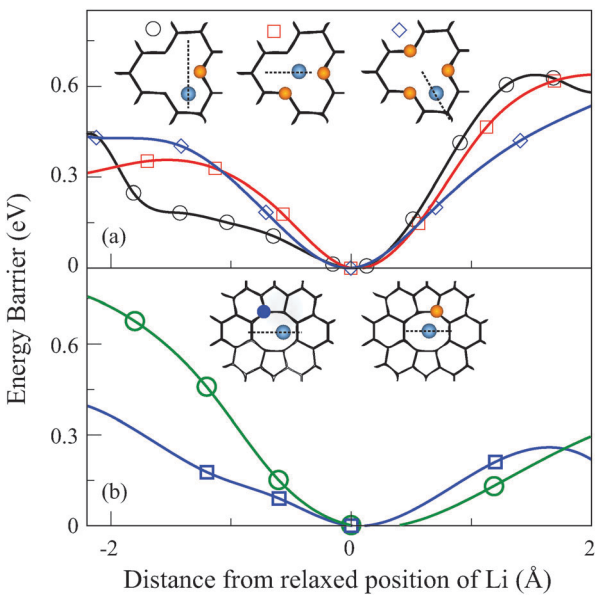

Fig. 4 (a) Li diffusion barriers and relaxed structure with Li for one (circles), two (squares) and three (diamonds) B doped mono-vacancy graphene. (b) Li diffusion barriers and relaxed structure with Li for one B doped (green circles) and one N doped (blue squares) di-vacancy graphene.

An opposite trend is observed in N-doped mono-vacancy. With increase in concentration of N at the defect the energy barriers increase, 0.95–1.75–2.62 eV for one, two, and three N doped mono-vacancy (Table 1), respectively. The contrasting nature of B and N doping can also be understood by looking at the Bader[48–50] charges on the C, B and N. The Bader charge analysis reveals that B tends to transfer all its charge to the C matrix, while N withdraws charge from the neighboring C atoms. In addition, Li also donates its charge partially. N doped graphene, being an electron rich system, does not accept electrons from Li leading to high energy barrier. On the other hand, the equal redistribution of charges to neighboring carbons in the B doped case and low Li adsorption energy lead to lowering of energy barriers in these structures.

Doped di-vacancy defects. We next study the effect of doping near di-vacancy defects. Fig. 4(b) shows a comparison of across diffusion barriers for the two best cases in di-vacancy doped graphene. Contrary to the B doped mono-vacancy case, the di-vacancy analogs depict high energy barriers. Our results indicate that the energy barriers of 0.59, 1.74, and 1.26 eV for two, three, and four B, respectively, are much higher than the B-doped mono-vacancy cases. The N doped di-vacancy graphene shows a similar behaviour, except in one N doped case where the barrier is 0.26 eV. Recent theoretical studies also suggest lowering of diffusion barriers for pyridinic N doped graphene.[51] Beyond one N doping in di-vacancy graphene, due to high adsorption energy, these structures act as a sink for Li.[35] In such cases, a large amount of energy associated with removal of Li from the lattice will be required, leading to high energy barriers.

In the case of B, the binding of Li to B is relatively weak, hence a consistent trend of low energy barriers is found. The highest and lowest energy barriers among all the B doped cases are 1.74 eV, and 0.31 eV for three B doped di-vacancy, and for two B doped mono-vacancy, respectively. The barriers for most of the N doped structures are consistently high, the highest being three N doped di-vacancy graphene.

3.2 Storage of Li within the defects

So far, we have only concentrated on the kinetics of a single Li atom based on which we have selected structures showing low energy barriers as possible candidates for anode materials. However, in reality, with a lot of Li ions diffusing in the battery, understanding of Li–Li interaction also needs to be addressed. This is also important to assess the feasibility of Li cluster formation, which is a major hurdle for the cyclic efficiency. The ease of adsorption of Li on a given structure directly influences the Li storage capacity of the anode material. In order to address these issues, we calculate the formation (adsorption) energy of Li, given as:

$$E_f(n) = E_{\text{system}+n\text{Li}} - E_{\text{system}} - nE_{\text{Li}} \quad (1)$$

where $E_{system+nLi}$, E_{system}, and E_{Li} refer to the total energies of structures with n number of Li, without Li and bulk (bcc) Li, respectively. For a stable structure, the lithiation energy should be within a window of ~ 2 eV[52] with respect to the Li cohesive energy.[53] Here the lithiation is studied as a sequential process, where we add one Li to the structure, upon relaxation of which we increment the number of Li. The subsequent difference in formation energies with n and $n + 1$ Li atoms ($E_f(n + 1) - E_f(n)$) gives incremental binding energy, a measure of the relative stability of the structure. The number of Li up to which the incremental binding energy is negative indicates the maximum number of Li uptake near the defects. We have referred to this number as the capacity of the defects, which is not the same as the specific capacity (expressed in mA h g^{-1}) of anode material. Since an increase in the Li/C ratio indicates greater capacity of the anode material,[54] we quantify the enhancement of storage of Li due to the presence of defects by the number of Li in the vicinity of the defects. Table 2 lists formation energies, starting from one Li to maximum Li uptake near a defect for all the structures studied in this work. Representative structures are shown in Fig. 5. Although the mono-vacancy defects can store up to four Li atoms as shown in Fig. 5(a), after two Li atoms the incremental binding energy becomes positive, indicating possible clustering of Li. Therefore, the maximum uptake capacity of mono-vacancy is concluded as two Li atoms. The enhanced capacity is due to strong interaction of Li with the unsatisfied bonds in mono-vacancy (as explained above). Both the di-vacancy (Fig. 5(d)) and Stone–Wales defects show a low capacity of only one Li per defect. Thus mono-vacancy graphene has the highest capacity among the un-doped defects in graphene.

Table 2 Capacity of un-doped, doped and defective doped graphene with formation energy (E_f) for all the systems with different number (n) of Li. We quote the capacity of each structure up to the maximum number of adsorbed Li in the vicinity of the defects

System	n	E_f	System	n	E_f
Pristine	1	0.71	Di	1	−0.55
	2	1.71			
Mono	1	−2.03	Stone–Wales	1	−0.76
	2	−2.72		2	−0.32
	3	−2.22			
	4	−1.69			
Pristine 1B	1	−1.40	Pristine 1N	1	0.75
Mono 1B	1	−2.30	Mono 1N	1	−1.69
	2	−1.98			
	3	−2.74			
Mono 2B	1	−0.36	Mono 2N	1	−1.64
	2	−1.40		2	−1.78
	3	−1.43			
Mono 3B	1	−1.20	Mono 3N	1	−3.28
	2	−1.96			
	3	−3.05			
Di 1B	1	−1.25	Di 1N	1	−1.30
Di 2B	1	−1.49	Di 2N	1	−3.06
				2	−4.92
Di 3B	1	−1.59	Di 3N	1	−3.31
				2	−4.49
Di 4B	1	−1.47	Di 4N	1	−3.54
				2	−4.57

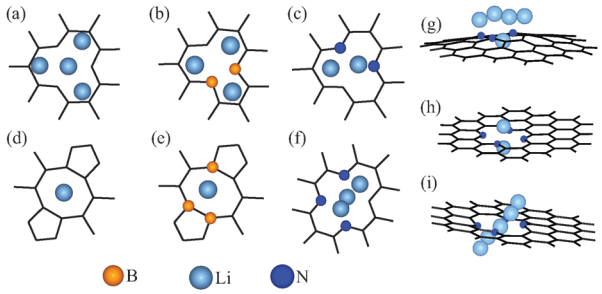

Fig. 5 Top view of relaxed structures of (a) mono-vacancy, (b) two B doped mono-vacancy, (c) two N doped mono-vacancy, (d) di-vacancy, (e) three B doped di-vacancy, and (f) three N doped di-vacancy structures with Li overloading. Side-view (g) three N (five Li) doped and (h) four N (two Li) and (i) four N (five Li) di-vacancy doped structures.

The capacity of one, two (Fig. 5(c)) and three N doped mono-vacancy is one, two and one, respectively. Similarly, the B doped mono-vacancy shows enhancement in capacity by adsorbing three Li atoms, (Fig. 5(b)). Increasing the concentration of B at the mono-vacancy does not change the capacity of doped mono-vacancy. On the other hand, the di-vacancy B doped graphene shows a capacity of only one Li. While single N doped di-vacancy can adsorb one Li atom, increasing the concentration of N (two, three, four) increases the number of adsorbed Li to two. Furthermore, as shown in Fig. 5(g–i), lithiation from one side of the plane of N doped di-vacancy, except for one N doped case where the Li sticks in the plane of graphene, causes a spontaneous diffusion of a few Li atoms to the other side of the plane. This can be attributed to high adsorption energies associated with these structures. Overall, in N doped di-vacancy, high adsorption energy together with stronger Li–Li interaction could make de-lithiation very difficult. Therefore, among all the structures studied, boron doped mono-vacancy can store a maximum number of (up to three) Li.

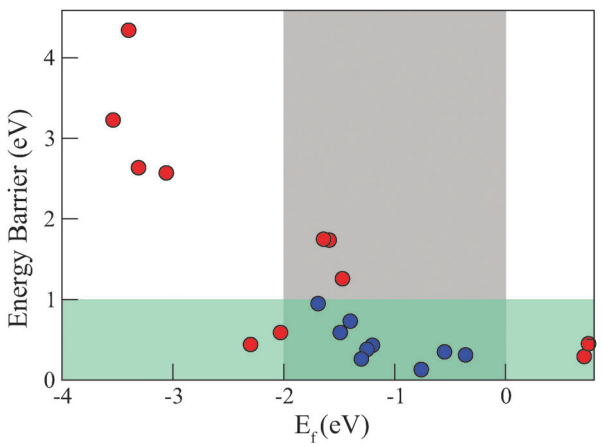

Fig. 6 Plot of diffusion energy barriers as a function of formation energy for all the systems studied. The green and gray shaded areas indicate optimal energy barriers (≤ 1 eV) and favorable formation energy window (~ 2 eV), respectively. The systems in the overlapped region, kinetically favor Li diffusion across the basal plane of graphene and have optimal adsorption energy for Li, are (from left to right) mono-1N, di-2B, pristine-B, di-1N, di-1B, mono-3B, Stone–Wales, di-vacancy, mono-2B and indicated by blue filled circles.

As apparent from the discussions so far, finding an optimal anode material requires simultaneous optimisation of adsorption energy, Li uptake capacity and low energy barriers. A plot of energy barriers as a function of corresponding adsorption energies is shown in Fig. 6. The shaded green and grey regions denote the range of optimal energy barriers and formation energy, respectively. The structures that fall in the overlapped region exhibit both low energy barriers and optimal adsorption energies, favourable for an anode material. Based on these criteria, structures indicated by blue circles, namely di-vacancy, Stone–Wales, pristine B doped, mono-vacancy doped with two, three B and one N, di-vacancy doped with one, two B, and one N, emerge as potential candidates for anode materials. The formation energy as a function of distance from the relaxed position of Li for all the promising cases varies by $\sim$10%, indicating that the Li will be mobile at room temperature. Furthermore, all these structures also show better Li uptake capacity than the pristine graphene, the best cases being boron doped mono-vacancy.

4 Conclusions

In conclusion, we have studied Li diffusion across the basal plane of doped and defective graphene and estimated the change in Li storage capacity. From the energy barrier calculation, we find that (i) di-vacancy, (ii) Stone–Wales, (iii) pristine B doped, (iv) B doped mono-vacancy, (v) one, two B doped di-vacancy, (vi) one N doped both mono-vacancy and di-vacancy give low energy barriers and lie within the optimal range of adsorption energy. From the calculation of capacity, we find that not all these structures having optimal binding energy and barrier show increase in Li uptake. Although N-doped defective graphene shows improved capacity, the high adsorption energy and barriers render it ineffective as anode material. Owing to the very low value of energy barrier and increased Li uptake, the B doped mono-vacancy graphene, in particular two B doped, emerges as a potential anode material for application in LIBs.

Acknowledgements

The authors thank the financial support from Korea Institute of Science and Technology (Grant No. 2E23920). We acknowledge Seungchul Kim for useful discussions. Kwang-Ryeol Lee and Sang Soo Han were supported by the Industrial Strategic Technology Development Program (Grant No. 10041589) funded by the Ministry of Knowledge Economy (MKE, Korea). We also thank the Materials Research Centre and Supercomputer Education and Research Centre, Indian Institute of Science, for computing facilities.

References

1 B. Kang and G. Ceder, *Nature*, 2009, **458**, 190–193.
2 M. Armand, S. Grugeon, H. Vezin, S. Laruelle, P. Ribière, P. Poizot and J.-M. Tarascon, *Nature Mater.*, 2009, **8**, 120–125.
3 M. Morcrette, P. Rozier, L. Dupont, E. Mugnier, L. Sannier, J. Galy and J.-M. Tarascon, *Nature Mater.*, 2003, **2**, 755–761.
4 K. Zaghib, A. Mauger, H. Groult, J. B. Goodenough and C. M. Julien, *Materials*, 2013, **6**, 1028–1049.
5 K. Kang, Y. S. Meng, J. Bréger, C. P. Grey and G. Ceder, *Science*, 2006, **311**, 977–980.
6 K. Persson, V. A. Sethuraman, L. J. Hardwick, Y. Hinuma, Y. S. Meng, A. van der Ven, V. Srinivasan, R. Kostecki and G. Ceder, *J. Phys. Chem. Lett.*, 2010, **1**, 1176–1180.
7 M. Winter, J. O. Besenhard, M. E. Spahr and P. Novk, *Adv. Mater.*, 1998, **10**, 725–763.
8 J.-M. Tarascon and M. Armand, *Nature*, 2001, **414**, 359–367.
9 Y. Nishi, *J. Power Sources*, 2001, **100**, 101–106.
10 P. Lian, X. Zhu, S. Liang, Z. Li, W. Yang and H. Wang, *Electrochim. Acta*, 2010, **55**, 3909–3914.
11 S. Yang, Y. Gong, Z. Liu, L. Zhan, D. P. Hashim, L. Ma, R. Vajtai and P. M. Ajayan, *Nano Lett.*, 2013, **13**, 1596–1601.
12 E. Yoo, J. Kim, E. Hosono, H.-s. Zhou, T. Kudo and I. Honma, *Nano Lett.*, 2008, **8**, 2277–2282.
13 D. Zhou, Y. Cui and B. Han, *Chin. Sci. Bull.*, 2012, **57**, 2983–2994.
14 E. Pollak, B. Geng, K.-J. Jeon, I. T. Lucas, T. J. Richardson, F. Wang and R. Kostecki, *Nano Lett.*, 2010, **10**, 3386–3388.
15 Y. Liu, V. I. Artyukhov, M. Liu, A. R. Harutyunyan and B. I. Yakobson, *J. Phys. Chem. Lett.*, 2013, **4**, 1737–1742.
16 X. Fan, W. T. Zheng, J.-L. Kuo and D. J. Singh, *ACS Appl. Mater. Interfaces*, 2013, **5**, 7793–7797.
17 X. Fan, W. Zheng and J.-L. Kuo, *Appl. Mater. Interfaces*, 2012, **4**, 2432–2438.
18 X. Zhao, C. M. Hayner, M. C. Kung and H. H. Kung, *ACS Nano*, 2011, **5**, 8739–8749.
19 X. Zhao, C. M. Hayner, M. C. Kung and H. H. Kung, *Adv. Energy Mater.*, 2011, **1**, 1079–1084.
20 J. M. Carlsson and M. Scheffler, *Phys. Rev. Lett.*, 2006, **96**, 046806.
21 P. Ayala, J. Reppert, M. Grobosch, M. Knupfer, T. Pichler and A. M. Rao, *Appl. Phys. Lett.*, 2010, **96**, 183110.
22 Y.-C. Lin, C.-Y. Lin and P.-W. Chiu, *Appl. Phys. Lett.*, 2010, **96**, 133110.
23 S. Wu, W. Ren, L. Xu, F. Li and H.-M. Cheng, *ACS Nano*, 2011, **5**, 5463–5471.
24 A. L. M. Reddy, A. Srivastava, S. R. Gowda, H. Gullapalli, M. Dubey and P. M. Ajayan, *ACS Nano*, 2010, **4**, 6337–6342.
25 L. S. Panchakarla, K. S. Subrahmanyam, S. K. Saha, A. Govindaraj, H. R. Krishnamurthy, U. V. Waghmare and C. N. R. Rao, *Adv. Mater.*, 2009, **21**, 4726–4730.
26 M. Endo, T. Hayashi, S.-H. Hong, T. Enoki and M. S. Dresselhaus, *J. Appl. Phys.*, 2001, **90**, 5670–5674.
27 M. Woińska, K. Milowska and J. Majewski, *Acta Phys. Pol., A*, 2012, **6**, 1087–1089.
28 M. Endo, C. Kim, K. Nishimura, T. Fujino and K. Miyashita, *Carbon*, 2000, **38**, 183–197.
29 L. Zhao, M. Levendorf, S. Goncher, T. Schiros, L. Plov, A. Zabet-Khosousi, K. T. Rim, C. Gutirrez, D. Nordlund, C. Jaye, M. Hybertsen, D. Reichman, G. W. Flynn, J. Park and A. N. Pasupathy, *Nano Lett.*, 2013, **13**, 4659–4665.

30 X. Li, D. Geng, Y. Zhang, X. Meng, R. Li and X. Sun, *Electrochem. Commun.*, 2011, **13**, 822–825.
31 X. Wang, Z. Zeng, H. Ahn and G. Wang, *Appl. Phys. Lett.*, 2009, **95**, 183103.
32 C. Kim, T. Fujino, T. Hayashi, M. Endo and M. S. Dresselhaus, *J. Electrochem. Soc.*, 2000, **147**, 1265–1270.
33 B. M. Way and J. R. Dahn, *J. Electrochem. Soc.*, 1994, **141**, 907–912.
34 F. Yao, F. Gne, H. Q. Ta, S. M. Lee, S. J. Chae, K. Y. Sheem, C. S. Cojocaru, S. S. Xie and Y. H. Lee, *J. Am. Chem. Soc.*, 2012, **134**, 8646–8654.
35 D. Das, S. Kim, K.-R. Lee and A. K. Singh, *Phys. Chem. Chem. Phys.*, 2013, **15**, 15128–15134.
36 G. Kresse and J. Hafner, *Phys. Rev. B: Condens. Matter Mater. Phys.*, 1993, **47**, 558–561.
37 G. Kresse and D. Joubert, *Phys. Rev. B: Condens. Matter Mater. Phys.*, 1999, **59**, 1758–1775.
38 P. E. Blóchl, *Phys. Rev. B: Condens. Matter Mater. Phys.*, 1994, **50**, 17953–17979.
39 J. P. Perdew, K. Burke and M. Ernzerhof, *Phys. Rev. Lett.*, 1996, **77**, 3865–3868.
40 G. Kresse and J. Furthmuller, *Comput. Mater. Sci.*, 1996, **6**, 15–50.
41 G. Henkelman, B. P. Uberuaga and H. Jónsson, *J. Chem. Phys.*, 2000, **113**, 9901.
42 J. Zheng, Z. Ren, P. Guo, L. Fang and J. Fan, *Appl. Surf. Sci.*, 2011, **258**, 1651–1655.
43 F. Banhart, J. Kotakoski and A. V. Krasheninnikov, *ACS Nano*, 2011, **5**, 26–41.
44 J. C. Meyer, C. Kisielowski, R. Erni, M. D. Rossell, M. F. Crommie and A. Zettl, *Nano Lett.*, 2008, **8**, 3582–3586.
45 A. Stone and D. Wales, *Chem. Phys. Lett.*, 1986, **128**, 501–503.
46 K. Suenaga, H. Wakabayashi, M. Koshino, Y. Sato, K. Urita and S. Iijima, *Nat. Nanotechnol.*, 2007, **2**, 358–360.
47 S. Flandrois, B. Ottaviani, A. Derre and A. Tressaud, *J. Phys. Chem. Solids*, 1996, **57**, 741–744.
48 W. Tang, E. Sanville and G. Henkelman, *J. Phys.: Condens. Matter*, 2009, **21**, 084204.
49 E. Sanville, S. D. Kenny, R. Smith and G. Henkelman, *J. Comput. Chem.*, 2007, **28**, 899–908.
50 G. Henkelman, A. Arnaldsson and H. Jónsson, *Comput. Mater. Sci.*, 2006, **36**, 354–360.
51 X. Kong and Q. Chen, *Phys. Chem. Chem. Phys.*, 2013, **15**, 12982–12987.
52 H. J. Hwang, J. Koo, M. Park, N. Park, Y. Kwon and H. Lee, *J. Phys. Chem. C*, 2013, **117**, 6919–6923.
53 B. J. Landi, M. J. Ganter, C. D. Cress, R. A. DiLeo and R. P. Raffaelle, *Energy Environ. Sci.*, 2009, **2**, 638–654.
54 V. Meunier, J. Kephart, C. Roland and J. Bernholc, *Phys. Rev. Lett.*, 2002, **88**, 075506.

